

SPGNet: A Shape-prior Guided Network for Medical Image Segmentation

Zhengxuan Song¹, Xun Liu², Wenhao Zhang³, Yongyi Gong⁴, Tianyong Hao⁵ and Kun Zeng^{1,*}

¹Sun Yat-sen University

²The Third Affiliated Hospital of Sun Yat-sen University

³University of the West of England

⁴Guangdong University of Foreign Studies

⁵South China Normal University

songzhx6@mail2.sysu.edu.cn, naturestyle@163.com, Wenhao.Zhang@uwe.ac.uk,
gongyongyi@gdufs.edu.cn, haoty@m.scnu.edu.cn, zengkun2@mail.sysu.edu.cn

Abstract

Given the intricacy and variability of anatomical structures in medical images, some methods employ shape priors to constrain segmentation. However, limited by the representational capability of these priors, existing approaches often struggle to capture diverse target structure morphologies. To address this, we propose SPGNet to guide segmentation by fully exploiting category-specific shape knowledge. The key idea is to enable the network to perceive data shape distributions by learning from statistical shape models. We uncover shape relationships via clustering and obtain statistical prior knowledge using principal component analysis. Our dual-path network comprises a segmentation path and a shape-prior path that collaboratively discern and harness shape prior distribution to improve segmentation robustness. The shape-prior path further serves to refine shapes iteratively by cropping features from the segmentation path, guiding the segmentation path and directing attention specifically to the edges of shapes which could be most significantly susceptible to segmentation error. We demonstrate superior performance on chest X-ray and breast ultrasound benchmarks.

1 Introduction

Medical image segmentation has always been critical to medical image processing. Currently, most mainstream methods focus primarily on high-precision pixel-level supervision. Despite significant achievements in a variety of segmentation tasks in differing domains, limitations persist when dealing with medical images. Primarily, anatomical structures in medical images often exhibit shape patterns and geometric information that generic pixel-level supervision could fail to leverage fully, especially when shape regularities are prominent and perceptibly advantageous.

Past studies indicate integrating shape prior knowledge could benefit traditional segmentation algorithms [Nosrati *et al.*, 2016]. For instance, introducing shape priors to level set

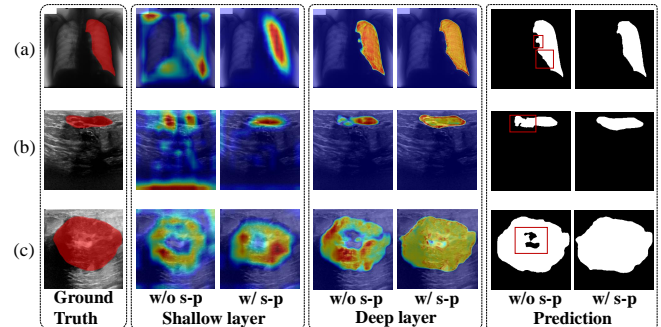


Figure 1: The first column shows the ground truth masks for a set of right lung X-rays, benign breast tumor ultrasound, and malignant tumor ultrasound images. The second to fifth columns present segmentation path visual attention maps in shallow encoder and deep decoder layers, without or with the collaborative shape-prior path. The sixth and seventh columns depict segmentation outputs with or without the shape-prior path. The network guided by shape priors demonstrates improved shape integrity and smoother edges.

contour evolution techniques proved to enhance the accuracy of segmentation [Chen *et al.*, 2002]. Integrating elastic shape priors into frameworks was also shown to be able to align the outcomes closer to the actual shape variations [Schoenemann *et al.*, 2007]. However, these conventional segmentation methods often struggle with complex medical image scenarios due to constraints in data distribution assumptions and susceptibility to noise and contextual information.

Deep learning methods, in comparison, exhibit greater flexibility in adapting to diverse shapes and backgrounds [Bohlander *et al.*, 2021]. It has been shown that this paradigm of segmentation methods could also benefit from shape priors to better cater for specific task requirements. For example, a model based on sparse representation and local repulsive deformation was proposed for normalizing the former deep convolutional neural network segmentation and constraining the segmentation results within an effective shape domain [Xing *et al.*, 2015]. Although post-processing has often demonstrated effective for further improving segmentation [Li *et al.*, 2017; Medley *et al.*, 2019], its usefulness still hinges on the dependability of the segmentation model. Another model [Lee *et al.*, 2019] based on template deformation implemented seg-

*Corresponding author

61 mentation by deforming the shape prior template. However,
62 this approach may be constrained by the expressiveness of the
63 priors and would likely be undermined by structural variations
64 in medical images, such as when handling images of various
65 organs with distinct shapes and morphological characteristics.

66 While these methods aim to constrain segmentation using
67 shape priors, they have not entirely endowed deep neural net-
68 works with the capacity to perceive shape patterns in the data.
69 We propose to enable deep learning methods to fully incor-
70 porate learned priors from training data as a form of regular-
71 ization. This enables segmentation networks to be influenced
72 by prior shape knowledge when classifying pixels. As shown
73 in Figure 1, with shape prior guidance, attention in shallow
74 layers concentrates completely on the target area. In deep
75 layers, the excellent alignment between the attention map and
76 the target area is maintained, while the most activated atten-
77 tion areas shift towards the edges which serves to improve
78 the accuracy and smoothness of segmentation. Conversely, a
79 network without guidance exhibits fragmented and misaligned
80 attention highly susceptible to noise and variability.

81 As shown in Figure 2, our end-to-end dual-path collabora-
82 tive network integrates a multi-class statistical shape model
83 for incorporating a wealth of shape priors. The segmenta-
84 tion path focuses on dense pixel-level classification, while the
85 shape-prior path regresses prior flows. We introduce a col-
86 laboration module establishing interactions between encoders
87 to enhance robustness by exchanging features. Simultane-
88 ously, by collaboratively learning multi-class statistical shape
89 model deformation, the segmentation encoder is enabled to
90 perceive shape distribution and utilise this explicit shape prior
91 knowledge to guide segmentation. We also use cropped local
92 features from the segmentation path to refine shapes across
93 different scales, guiding attention to focus on boundaries.

94 Our contributions are summarized as follows:

- 95 • We propose a novel dual-path collaborative segmentation
96 network, SPGNet, which embeds explicit and diverse
97 shape priors. The dual-path structure enhances the repre-
98 sentation capability of segmentation path encoders. The
99 segmentation path, guided by the explicit shape priors,
100 reinforces shape understanding and enhances attention at
101 target edges, addressing single-path deficiencies in cap-
102 turing shape features. We also design a cluster strategy
103 to learn shape regularities from the training set.
- 104 • We explore the collaborative effects of SPGNet and
105 demonstrate the effectiveness of the shape-prior path
106 in improving segmentation accuracy. Specifically, we
107 validate the efficacy of each component within the shape-
108 prior path.
- 109 • We evaluate SPGNet on a chest X-ray dataset with promi-
110 nent shape regularities and a breast ultrasound dataset
111 with potential regularities. Results demonstrate superior
112 accuracy over baselines and existing state-of-the-art meth-
113 ods, particularly in edge smoothness. We also validate its
114 adaptability to medical images with low signal-to-noise
115 ratios, blurry boundaries, and significant shape and posi-
116 tional variations of lesions. The superiority of our method
117 has been demonstrated.

2 Relate Works 118

Shape Clustering and Statistical Modeling. Shape clus- 119
tering groups shapes by extracting descriptors and clustering 120
based on similarity distances. For instance, a skeleton-based 121
approach captures intrinsic structural information for same- 122
class shapes, clustering using a node-matching matrix [Shen 123
et al., 2013]. However, skeleton-based methods often express 124
relatively coarse shape features. In contrast, a hierarchical clus- 125
tering method is used in a different study for contour-based 126
shapes to learn probabilistic models from shape clusters [Sri- 127
vastava *et al.*, 2005]. In another approach, to address unlabeled 128
longitudinal shape data, a flexible nonlinear mixture model 129
is established by learning average shape trajectories and vari- 130
ances for each cluster [Debavalaere *et al.*, 2020]. For instance 131
segmentation, k-means clustering of training masks are used 132
to obtain centres of shape clusters, establishing a linear prior 133
model e.g., [Kuo *et al.*, 2019]. A pipeline combining segmen- 134
tation, clustering, and modeling has also been proposed [Bruse 135
et al., 2017]. With the rise of deep neural networks, exploring 136
clustered shape information with statistical models still has 137
significant potential. 138

Shape-prior Guided Segmentation. Numerous methods 139
have attempted to leverage shape priors for segmentation. For 140
example, to address blurred overlapping regions in the cell 141
cytoplasm, a generator utilizing a prior template to generate 142
masked was proposed [Song *et al.*, 2020]. Similarly, a cyclic 143
registration network was also designed to integrate anatomi- 144
cal context specificity with priors [Jiang and Veeraraghavan, 145
2022]. For a different medical application, a deep neural net- 146
work was designed to predict PCA layers for improving the 147
segmentation of the left ventricle in ultrasound images [Mil- 148
letari *et al.*, 2017]. Generating threshold-based priors and 149
optimizing outputs via a spatial transform network was also 150
proposed as another strategy for harnessing prior shape knowl- 151
edge [Zhao *et al.*, 2021]. More recently, it was also found that 152
introducing an additional branch transforms visible regions 153
into complete areas through supervision, and therefore facili- 154
tates holistic shape understanding [Gao *et al.*, 2023]. Similarly, 155
another study proposed a generative invariant shape prior net- 156
work that introduced a branch to learn invariant priors, mimick- 157
ing human perceptual learning of basic shapes [Li *et al.*, 2023]. 158
Other than considering two-dimensional shapes, a different 159
method used three-dimensional reconstructed shapes as priors 160
and reconstructed occluded objects before projecting them 161
to predict complete mask [Li *et al.*, 2022]. However, these 162
methods may struggle to handle complex and heterogeneous 163
targets due to insufficient shape diversity [Zhao *et al.*, 2021; 164
Jiang and Veeraraghavan, 2022]. Implicit priors may fail to 165
generalize [Gao *et al.*, 2023; Li *et al.*, 2023]. In contrast, our 166
approach establishes an explicit multi-class shape statistical 167
model to guide segmentation. 168

3 Methodology 169

3.1 Overview 170

In Figure 2, we introduce SPGNet, a novel image segmen- 171
tation algorithm with embedded shape priors. Section 3.2 172
discusses offline multi-class shape statistical modeling, Sec- 173

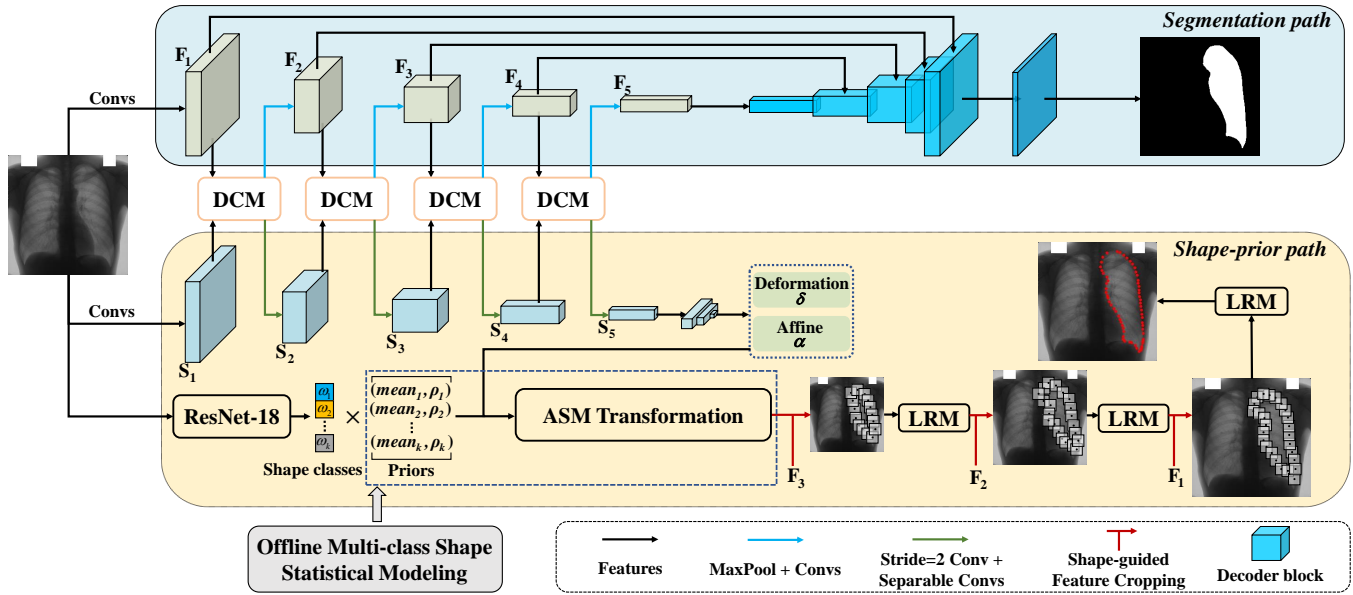


Figure 2: SPGNet is a dual-path collaborative network consisting of three main components: offline multi-class shape statistical modeling, segmentation path, and shape prior path.

tion 3.3 details SPGNet’s internal modules and Section 3.4 introduces the hybrid loss function for network training.

3.2 Offline Multi-class Shape Statistical Modeling

Shape Preparation. As shown in Figure 3, we derive shape data from mask annotations, focusing on regions with heightened curvature to build a statistical model with prominent shape features. The shape generation process involves: (i) Employing Bézier curves to smoothly fit mask contours, yielding a set of smoothed contour points. (ii) Determining the number of sampling points as p and calculating the absolute curvature for each point, followed by normalization. A base value is introduced to prevent neglecting points with extremely small curvature. The ratio of the sum of normalized curvatures to the number of sampling points serves as the sampling distance. (iii) Iterating through contour points, saving the current sum of curvatures and the number of sampled points, denoted as k . When the sum exceeds k times the sampling distance, the point is saved as a sample point and k increments by 1. The traversal ends when k reaches p . The sampled p points constitute the shape contour, represented as $S^i = ((x_1^i, y_1^i), \dots, (x_p^i, y_p^i))^T \in \mathbb{R}^{p \times 2}$.

Procrustes Shapes Agglomerative Clustering. We employed the agglomerative clustering method, utilizing the Procrustes shape distance as the shape similarity metric, which requires aligning shapes before computing distances. The Procrustes shape distance calculation between two aligned shapes S^1 and S^2 is calculated by:

$$P_d = \sqrt{\sum_{j=1}^p [(x_j^1 - x_j^2)^2 + (y_j^1 - y_j^2)^2]} \quad (1)$$

In Figure 3, the agglomerative clustering of shapes involves these steps: (i) Standardizing and aligning all shapes using

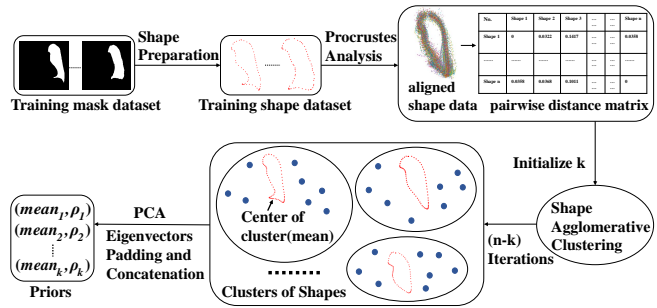


Figure 3: This is the flowchart depicting the process of computing multi-class shape priors.

the Procrustes analysis [Cootes *et al.*, 1995] in the training set. (ii) Calculating the pairwise distance matrix using Procrustes shape distance. (iii) Determining the number of clusters k . Starting with $k = 2$ and iteratively incrementing k , we select the k value that maximizes the variance of distances between k cluster centers as the initialization. We limit k to a maximum of 100 to prevent excessive redundancy in categories. (iv) Initiating agglomerative clustering with complete linkage for calculating inter-cluster distances, minimizing dissimilar shape aggregation between clusters. After all iterations, we obtain k shape clusters.

Multi-class Shape Priors and Modeling. We compute the mean shape within each cluster and conduct principal component analysis (PCA) on cluster shapes to derive eigenvectors representing major variations. The number of eigenvectors per cluster aligns with the maximum across clusters, denoted as t . Concatenating mean shapes and eigenvectors yields shape priors, denoted as $Priors = \{(mean_i, \rho_i)\}_{i=1}^k \in \mathbb{R}^{k \times (1+t) \times p \times 2}$. Simultaneously, shape category labels C are

222 obtained from the shape clusters. The Active Shape Model
 223 (ASM) [Cootes *et al.*, 1995], a statistical model for shapes, nec-
 224 essitates a set of shape training samples $Set = \{(S^i)_{i=1}^n\}$ for
 225 model construction. Initially, we compute the average shape
 226 vector for all shapes:

$$\bar{S} = \frac{1}{n} \sum_{i=1}^n S^i \quad (2)$$

227 We employ PCA for dimensionality reduction on the n
 228 shape training samples, creating an approximate model that
 229 encapsulates the entire training dataset:

$$S \approx \bar{S} + b\Phi \quad (3)$$

230 where $\Phi = (\rho_1, \rho_2, \dots, \rho_j) \in \mathbb{R}^{j \times p \times 2}$ represents the first j
 231 major eigenvectors corresponding to the eigenvalues of the
 232 covariance matrix. $b \in \mathbb{R}^{1 \times j}$ denotes the shape deformation
 233 parameters. Subsequently, we can utilize a neural network to
 234 predict the deformation parameters b , facilitating the fitting
 235 of the shape statistical model to the shapes in the training set.
 236 Additionally, we introduce an affine transformation function a
 237 with parameters $\gamma = (s_\gamma, \theta_\gamma, (t_1)_\gamma, (t_2)_\gamma) \in \mathbb{R}^{1 \times 4}$. The four
 238 parameters include the scale parameter s_γ , rotation parameter
 239 θ_γ , and translation parameters $(t_1)_\gamma$ and $(t_2)_\gamma$. For a set of
 240 points $S = (S_x, S_y) \in \mathbb{R}^{p \times 2}$, affine transformations can be
 241 described as:

$$a(S, \gamma) = \begin{bmatrix} s_\gamma \cos(\theta_\gamma) & -s_\gamma \sin(\theta_\gamma) & (t_1)_\gamma \\ s_\gamma \sin(\theta_\gamma) & s_\gamma \cos(\theta_\gamma) & (t_2)_\gamma \end{bmatrix} \begin{bmatrix} S_x \\ S_y \\ 1 \end{bmatrix} \quad (4)$$

242 In summary, an ASM Transformation model is denoted as:

$$T_{asm}(\bar{S}, \Phi, \gamma, b) = a(\bar{S} + b\Phi, \gamma) \quad (5)$$

243 The ASM Transformation function is embedded in the net-
 244 work computational process. *Priors* are precomputed offline
 245 before training and inference, entering the network as constant
 246 parameters.

247 3.3 SPGNet

248 **Dual-path Collaboration Module(DCM).** In the encoder
 249 sections of both paths, we aim for mutual attention during
 250 training, allowing the segmentation path to attend to learned
 251 features from the shape-prior path and vice versa. To achieve
 252 this, we introduce the dual-path collaboration module (DCM),
 253 incorporating spatial and channel attention for enhanced fea-
 254 ture interaction. As shown in Figure 4, the DCM takes features
 255 $F_i \in \mathbb{R}^{C_i \times H_{F_i} \times W_{F_i}}$ and $S_i \in \mathbb{R}^{C_i \times H_{S_i} \times W_{S_i}}$ from the two
 256 paths as input, with S_i resized to match F_i dimensions. Spatial
 257 attention is computed by averaging along the channel dimen-
 258 sion and applying the sigmoid activation function $\sigma(\cdot)$. For
 259 channel attention, global average pooling (GAP) is applied
 260 along the spatial dimension, and linear layers, along with the
 261 sigmoid activation function $\sigma(\cdot)$, calculate channel attention.
 262 The concatenated features, after passing through consecutive
 263 convolutional layers, are multiplied separately by spatial at-
 264 tention and channel attention, before the results are summed.
 265 This process introduces spatial and channel attention, fostering
 266 interactive features. A residual structure combines these in-
 267 teractive attention features with features from each path. The
 268 resulting features F_{i+1} and S_{i+1} are obtained after passing
 269 through the encoder blocks of each path.

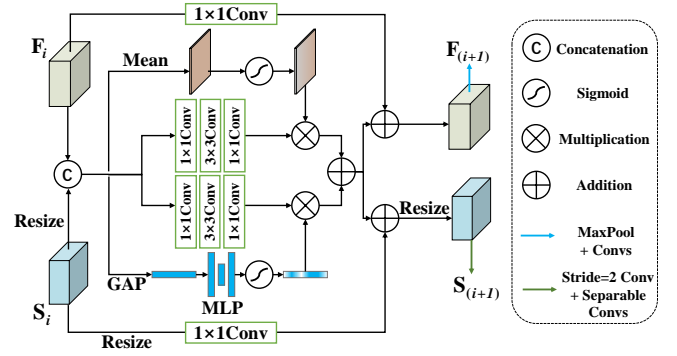


Figure 4: The structure of the Dual-path Collaboration Module (DCM).

270 **Segmentation Path.** In Figure 2, the segmentation path em-
 271 ploys an encoder-decoder architecture with skip connections.
 272 All subsequent encoder blocks, except the initial one, receive
 273 interactive attention features from the DCM. Each encoder
 274 block is composed of two sets of sub-blocks and a max-pooling
 275 layer. The sub-blocks include a convolutional layer, ReLU
 276 activation and batch normalization. In the decoder section,
 277 features from the preceding layer are initially upsampled us-
 278 ing bilinear interpolation. Following concatenation with the
 279 skip connection input from the encoder, the combined fea-
 280 tures enter the decoder. The ultimate layer of the decoder em-
 281 ploys a convolutional layer to derive the probability distribution map
 282 for dense pixel-wise classification.

283 **ASM Transformation.** We acquired prior shape knowledge,
 284 denoted as *Priors*, which is loaded into the network before
 285 training. We utilised the ResNet18 [He *et al.*, 2016] as the
 286 shape classifier backbone in the classification network. During
 287 training, the classifier learns the shape category weights for
 288 input images, and the appropriate shape prior is obtained by
 289 multiplying the classifier output $Classes \in \mathbb{R}^k$ with *Priors*.
 290 Specifically, the classifier output is used to calculate the shape
 291 mean $mean \in \mathbb{R}^{1 \times p \times 2}$ and t eigenvectors $\rho \in \mathbb{R}^{t \times p \times 2}$.
 292 In the shape-prior path, the shape encoder block employs a com-
 293 bination of spatially separable convolution and convolutional
 294 layers with a stride of 2, focusing on capturing edge and shape
 295 features. The output of the last encoder block is fed through
 296 continuous convolutional layers to obtain deformable param-
 297 eters $\delta \in \mathbb{R}^{1 \times t}$ and affine parameters $\alpha \in \mathbb{R}^{1 \times 4}$. The shape L^0
 298 is obtained through ASM Transformation:

$$L^0 = T_{asm}(mean, \rho, \alpha, \delta) \quad (6)$$

299 **Shape-guided Feature Cropping.** As illustrated in Figure
 300 5, given the input shape points $L^{(t-1)} \in \mathbb{R}^{p \times 2}$ and the fea-
 301 tures $F_{(4-t)}$ from the segmentation path, where $t = 1, 2, 3$,
 302 and setting the relative length of the clipping patch l , we first
 303 convert $F_{(4-t)}$ into $f_{(4-t)} \in \mathbb{R}^{c \times w_{f_{(4-t)}} \times h_{f_{(4-t)}}}$ through con-
 304 volution. For a shape point in the spatial direction of $f_{(4-t)}$,
 305 denoted as (L_x^{t-1}, L_y^{t-1}) , we clip out c patches, each contain-
 306 ing $n \times n$ sampled feature points. The feature at each sampled
 307 point is calculated on $f_{(4-t)}$ using bilinear interpolation, and
 308 we retain the bottom-left relative position coordinates of the
 309 patch, denoted as $(L_x^{t-1}, L_y^{t-1})_{lt}$. By using p shape points, we

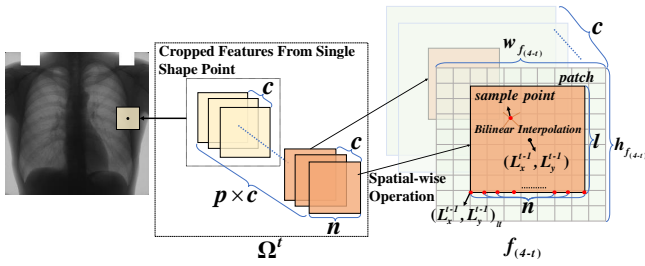


Figure 5: Shape-guided Feature Cropping

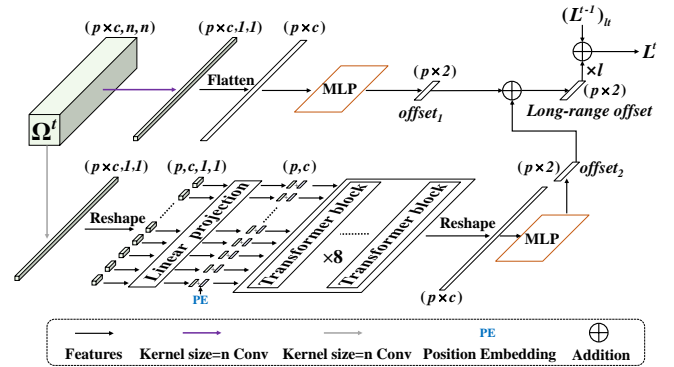


Figure 6: The structure of the Long-range Refinement Module (LRM)

310 obtain the clipped feature sequence $\Omega^t \in \mathbb{R}^{(p \times c) \times n \times n}$ and the
311 bottom-left position sequence $L_{lt}^{t-1} \in \mathbb{R}^{p \times 2}$.

312 **Long-range Refinement Module(LRM).** The global correlation of shape points is crucial for accuracy. In Figure 6, we
313 introduce the Long-range Refinement Module (LRM), which takes Ω^t , L_{lt}^{t-1} , and the patch side length l as inputs. This facilitates the adjustment of shape points within the patch. LRM
314 consists of a parallel structure employing convolution and a multilayer perceptron. Additionally, it utilizes a transformer encoder [Zheng *et al.*, 2021] to handle the feature sequence. In
315 the first direction, a $n \times n$ convolutional layer extracts global features from Ω^t , followed by flattening and passing through a multilayer perceptron with two linear layers and ReLU activation,
316 resulting in $offset_1 \in \mathbb{R}^{p \times 2}$. In the second direction, another $n \times n$ convolutional layer extracts Ω^t and projects it onto token sets with positional embedding. Afterwards, an
317 8-layer transformer encoder with multi-head self-attention is employed to establish global feature correlations. The output, reshaped into linear features, passes through a multilayer perceptron,
318 yielding $offset_2 \in \mathbb{R}^{p \times 2}$. The refined shape points are computed as follows:
319
320
321
322
323
324
325
326
327
328
329
330

$$L^t = L_{lt}^{(t-1)} + (offset_1 + offset_2) \times l \quad (7)$$

331 In our model, the coarse output of the ASM Transformation is denoted as L^0 , and the outputs of the three stages of LRM are (L^1, L^2, L^3) .

3.4 Hybrid Loss Function

335 We formulated a hybrid loss function for training SPGNet. The total loss \mathcal{L} is a weighted sum of the segmentation loss \mathcal{L}_{seg} derived from the segmentation path and the shape loss \mathcal{L}_{shape} , along with the classification loss \mathcal{L}_c . The segmentation loss is calculated as follows:
336
337
338
339

$$\mathcal{L}_{seg} = \lambda_1 \mathcal{L}_{ce}(\hat{Y}, Y) + \lambda_2 \mathcal{L}_{dice}(\hat{Y}, Y) \quad (8)$$

340 where \hat{Y} is the output probability segmentation map from our segmentation path, and Y represents the ground truth for the probability segmentation mask. The losses \mathcal{L}_{ce} and \mathcal{L}_{dice} correspond to the cross-entropy and dice loss [Li *et al.*, 2019], respectively. The classification loss is calculated as:
341
342
343
344

$$\mathcal{L}_c = \lambda_3 \mathcal{L}_{bce}(\hat{C}, C) \quad (9)$$

345 where \hat{C} represents the predicted shape category probabilities from classifier, and C refers to the ground truth for shape categories. \mathcal{L}_{bce} corresponds to the binary cross-entropy
346
347

348 loss [Chen *et al.*, 2023]. The shape loss calculation is as follows:
349

$$\mathcal{L}_{shape} = \sum_{i=4}^7 \lambda_i \mathcal{L}_{l1}(L^{i-4}, L) \quad (10)$$

350 where L represents the ground truth for the shape, and \mathcal{L}_{l1} refers to the L1 loss [Feng *et al.*, 2018]. The total loss \mathcal{L} is defined as:
351
352

$$\mathcal{L} = \mathcal{L}_{seg} + \mathcal{L}_c + \mathcal{L}_{shape} \quad (11)$$

4 Experiment

4.1 Dataset and Pre-Processing

353 In our comprehensive evaluation, we utilized two publicly available datasets: chest X-rays and breast ultrasound image data. Below, we outline the databases employed for these experiments.
354
355
356
357
358

359 **JSRT Dataset.** The JSRT database [Shiraishi *et al.*, 2000] consists of 247 high-resolution X-ray images, comprising 154 conventional chest X-rays with lung nodules selected from 14 medical centers and 93 chest X-rays without lung nodules. The dataset provides manually annotated masks for three anatomical structures of interest: the left lung, right lung, and heart. We separated the masks for these three anatomical structures for individual evaluations.
360
361
362
363
364
365
366

367 **Breast Ultrasound Dataset (BUS).** The Breast Ultrasound Dataset (BUS) [Al-Dhabyani *et al.*, 2020] includes 780 breast ultrasound images categorized into three classes: 133 normal, 437 benign, and 210 malignant images. For our experiments, we combined samples from both benign and malignant classes. The dataset offers manually annotated masks for tumor regions.
368
369
370
371
372
373

4.2 Implementation Details and Metrics

374 We implemented all evaluation methods on a server equipped with an NVIDIA GeForce RTX 4090 GPU. For a fair quantitative comparison, all methods for dense pixel-level classification underwent evaluation using the same 5-fold cross-validation scheme, maintaining a standardized input resolution of 256×256 . To prevent overfitting, consistent data augmentation was applied in experiments, including random rotation,
375
376
377
378
379
380
381

Method	Left Lung			Right Lung			Heart		
	Dice \uparrow	Jaccard \uparrow	HD95 \downarrow	Dice \uparrow	Jaccard \uparrow	HD95 \downarrow	Dice \uparrow	Jaccard \uparrow	HD95 \downarrow
UNet [Ronneberger <i>et al.</i> , 2015]	97.87	95.87	5.06	97.26	94.72	5.92	95.63	91.70	9.48
AttUNet [Oktay <i>et al.</i> , 2018]	97.88	95.87	4.57	97.32	94.83	5.71	95.72	91.88	8.34
UNet++ [Zhou <i>et al.</i> , 2020]	97.91	95.94	4.35	97.27	94.74	5.58	95.63	91.71	8.88
TransUNet [Chen <i>et al.</i> , 2021]	97.53	95.20	5.76	96.87	93.99	7.34	94.85	90.31	10.77
SAUNET [Sun <i>et al.</i> , 2020]	97.64	95.90	4.51	96.89	94.03	7.00	95.01	90.57	8.71
SPGNet_{seg}(ours)	98.01	96.10	3.91	97.40	95.01	5.64	95.96	92.27	8.09
<hr/>									
HybridGNet+2IGSC [Gaggion <i>et al.</i> , 2022]	93.51	87.9	8.64	91.72	84.82	11.45	90.05	82.11	12.12
Joint+HDC [Bransby <i>et al.</i> , 2023]	95.83	92.05	6.78	94.84	90.29	8.70	93.14	87.28	9.83
SPGNet_{shape}(ours)	97.39	94.93	4.57	97.28	94.73	5.62	94.97	90.33	9.95

Table 1: Comparison with state-of-the-art methods on JSRT. Above the central horizontal line, a comparison is made for methods based on dense pixel-level classification, while below, a comparison is conducted for methods based on points regression.

Method	Breast Tumor		
	Dice \uparrow	Jaccard \uparrow	HD95 \downarrow
UNet [Ronneberger <i>et al.</i> , 2015]	73.15	63.89	43.2
AttUNet [Oktay <i>et al.</i> , 2018]	74.60	66.05	30.25
UNet++ [Zhou <i>et al.</i> , 2020]	72.94	64.52	31.76
TransUNet [Chen <i>et al.</i> , 2021]	71.84	62.66	38.27
SAUNET [Sun <i>et al.</i> , 2020]	73.52	65.00	31.28
UNext-L [Valanarasu <i>et al.</i> , 2022]	67.03	56.73	46.11
AAUNet [Chen <i>et al.</i> , 2023]	77.68	68.94	29.10
SPGNet_{seg}(ours)	78.40	69.70	26.46

Table 2: Comparison with state-of-the-art methods based on dense pixel-level classification on BUS.

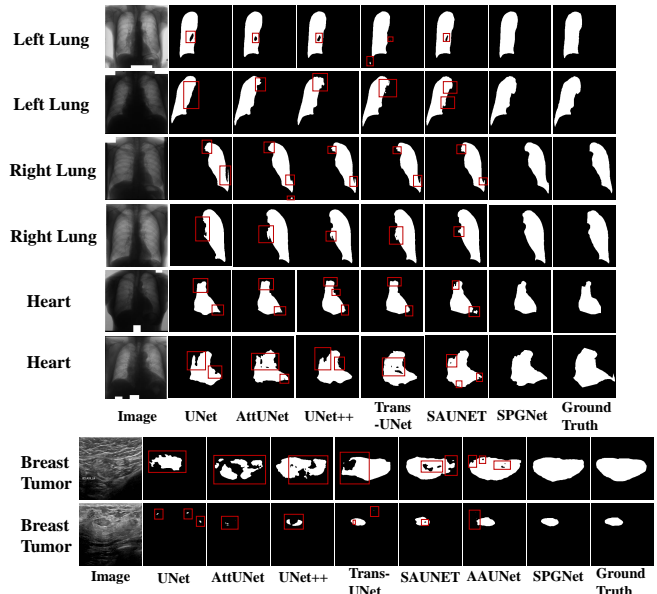


Figure 7: Qualitative experimental examples were conducted on the BUS and JSRT datasets, where errors in the comparative method are highlighted with red rectangular boxes.

382 random vertical flipping, and random changes in brightness
383 and contrast. We performed 150 epochs of training on the
384 JSRT dataset and 300 epochs on the Breast Ultrasound Dataset
385 (BUS) while keeping the remaining training hyperparameters
386 consistent. The batch size was set to 16, utilizing the Adam
387 optimizer. The initial learning rate was 0.0001, with weight
388 decay at 0.0005, and a learning rate decay of 90% every 15
389 epochs. During the validation phase, we assessed segmenta-
390 tion performance using the Dice coefficient(%) (Dice), Jac-
391 card index(%) (Jaccard), and 95% Hausdorff Distance(mm)
392 (HD95).

4.3 Comparison with State-of-the-art

394 **Results on JSRT.** Table 1 summarizes the experimental out-
395 comes for the left lung, right lung, and heart components in
396 JSRT. Our method, employing a shape point sampling of 128,
397 surpasses other dense pixel-level classification approaches in
398 the average Dice score. Although the improvement in average
399 Dice may not be as pronounced compared to other methods,
400 as depicted in Figure 7, our approach distinctly excels in edge
401 smoothness and accuracy. Moreover, in methods based on
402 points regression, our approach (with a shape point sampling
403 of 64) achieves significantly higher average Dice scores in
404 the shape path than other state-of-the-art points regression
405 methods. Training was conducted in both scenarios, using
406 our parameters and the optimal parameters specified in their
407 respective papers. Compared to the state-of-the-art method
408 [Bransby *et al.*, 2023], our method demonstrates improve-
409 ments in Dice scores of 1.56%, 2.44%, and 1.83% for the
410 left lung, right lung, and heart, respectively. These results

highlight the superior performance of SPGNet on datasets 411
exhibiting prominent shape patterns. 412

Results on BUS. Table 2 presents the experimental re- 413
sults on the BUS dataset. The segmentation path of our 414
method(with a shape point sampling of 128) achieved an av- 415
erage Dice score superior to other state-of-the-art methods 416
based on dense pixel-level classification. For SPGNet, the 417
Dice and Jaccard scores reached 78.4% and 69.7%, respec- 418
tively, This represents an improvement of 0.72% and 0.76% 419
compared to the previous state-of-the-art method [Chen *et* 420
al., 2023]. As illustrated in Figure 7, our method excels in 421
accurately identifying the location of breast tumors and main- 422
taining overall shape and edge smoothness. The experimental 423
results demonstrate that SPGNet can leverage shape priors 424
to enhance performance on datasets with underlying shape 425
patterns. 426

Method	\mathcal{L}_{seg}	\mathcal{L}_c	\mathcal{L}_{shape}	Dice of BUS	Dice of Right Lung
Baseline	-	-	-	74.04	97.49
DCM	$\lambda_1 \lambda_2$	-	-	75.69	97.52
DCM+ T_{asm}	$\lambda_1 \lambda_2$	λ_3	λ_4	78.56	97.64
DCM+ T_{asm} + (Crop+LRM) $\times 1$	$\lambda_1 \lambda_2$	λ_3	$\lambda_4 \lambda_5$	78.86	97.66
DCM+ T_{asm} + (Crop+LRM) $\times 2$	$\lambda_1 \lambda_2$	λ_3	$\lambda_4 \lambda_5 \lambda_6$	79.37	97.69
DCM+ T_{asm} + (Crop+LRM) $\times 3$	$\lambda_1 \lambda_2$	λ_3	$\lambda_4 \lambda_5 \lambda_6 \lambda_7$	79.63	97.71

Table 3: Ablation study on the effectiveness of components in the shape-prior path, with fold 1 of the BUS dataset and fold 4 of JSRT(right lung) as the validation set.

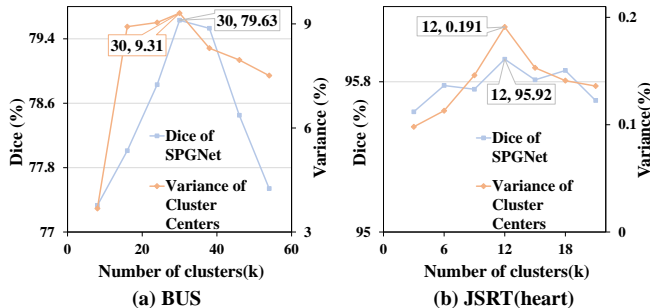


Figure 8: Ablation on the number of clusters in BUS and JSRT (Heart), with fold 1 of the BUS and JSRT as the validation set.

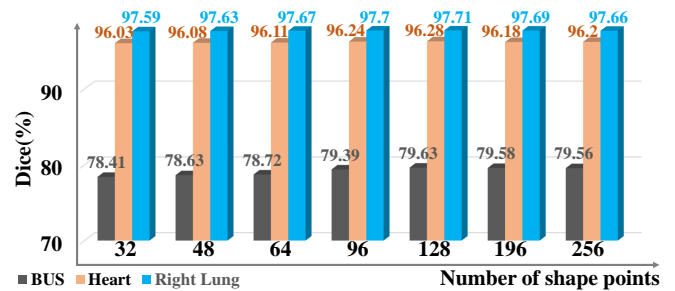


Figure 9: Ablation on the number of shape points in BUS and JSRT (Heart) was performed, with fold 1 of BUS, fold 3 of JSRT (Heart) and fold 4 of JSRT (Right Lung) as the validation sets.

lung, respectively, compared to the result of (DCM+ T_{asm}). This demonstrates that our combination of multi-stage shape refinement modules (Crop+LRM) is effective. The experimental results indicate that the shape-prior path could lead to improved performance in the segmentation path.

Ablation on the Number of Clustering. We validated the impact of the number of clusters in Procrustes shapes agglomerative clustering on segmentation performance. Our criterion is to select the value that maximizes the variance of cluster distances as the offline clustering quantity for SPGNet. As shown in [Figure 8 (a)], when we chose the clustering quantity k value according to our rule (our rule selected 30), the variance of cluster centers reached 9.31%, and SPGNet achieved a dice value of 79.63%. The segmentation performance is higher compared to situations when we chose the values of the cluster of numbers (k) around the one selected according to our criterion. A similar trend can be observed in [Figure 8(b)]. This suggests that selecting the value that maximizes the variance of cluster distances can approximate an optimal quantity of shape types, avoiding situations with insufficient categories or redundancy. This serves as a suitable rule for selecting the clustering quantity to enhance segmentation performance.

Ablation on the Number of Shape Points. We assessed the impact of varying quantities of shape points on segmentation performance, as depicted in Figure 9. Seven scenarios, ranging from 32 to 256 shape points, were selected to observe their influence on segmentation performance. As the number of shape points increased, our segmentation performance gradually improved, reaching optimal performance at 128 points. It can be observed that the number of points (e.g., 96, 128, 192, 256) that effectively represent shapes leads to a significant improvement in model performance, with little variation among them. Therefore, selecting sufficient and reasonable numbers of points can better promote model performance improvement.

5 Conclusion

In this paper, we introduce a novel shape-prior guided segmentation network. The core concept is to enable the network to grasp the shape distribution within the data by learning from statistical shape model enriched with shape prior knowledge, thereby enhancing segmentation accuracy. We validate the effectiveness of the proposed network through extensive experiments on two public datasets.

4.4 Ablation Study

Ablation of Each Component in Shape-prior Path. Table 3 illustrates the performance enhancement trends of the segmentation path with the introduction of each component in our dual-path collaborative network compared to the baseline. To validate each module, various coefficients in the mixed loss function were adjusted to reflect the combined effects. It was observed that three factors primarily contributed to the improvement: (i) DCM (Dual-path Collaboration Module): Coefficients λ_1 and λ_2 for \mathcal{L}_{seg} were set during training to highlight the impact of DCM. Utilizing DCM, which enables collaborative learning of input image features by dual-path encoders, yielded enhancements of 1.65% for BUS and 0.03% for the right lung, emphasizing the effectiveness of our dual-path collaborative network structure. (ii) Supervision on Shape: Building upon the first factor (DCM), coefficients λ_3 and λ_4 for \mathcal{L}_c and \mathcal{L}_{shape} were introduced. This supervises the shape weights and guides the ASM Transformation output shape, leading to a significant 2.87% improvement for BUS and 0.12% for the right lung. This underscores the effectiveness of our offline-modeled, multi-class shape priors in guiding the segmentation network, demonstrating that deep learning segmentation networks, guided by diverse shape prior information, can significantly compensate for deficiencies in shape perception. (iii) Multi-stage Shape Refinement: Building upon the second factor (DCM+ T_{asm}), coefficients λ_5 , λ_6 , and λ_7 were sequentially introduced for each stage of shape refinement. With the introduction of each refinement stage, there has been a relative improvement of 0.3%, 0.81% and 1.07% for BUS, and 0.02%, 0.05% and 0.07% for the right

499 Acknowledgments

500 This study was supported by grants from the National Nat-
501 ural Science Foundation of China (Grant No. 81873631,
502 81370866, 81070612), Guangzhou Science and Technology
503 Planning Project (Grant No. 202002020047), and Guangdong
504 Basic and Applied Basic Research Foundation (Grant No.
505 2019A1515011078), and the Royal Society (Grant Reference:
506 IEC\NSFC\201041).

507 References

- 508 [Al-Dhabyani *et al.*, 2020] Walid Al-Dhabyani, Mohammed
509 Gomaa, Hussien Khaled, and Aly Fahmy. Dataset of breast
510 ultrasound images. *Data in brief*, 28:104863, 2020.
- 511 [Bohlender *et al.*, 2021] Simon Bohlender, Ilkay Oksuz, and
512 Anirban Mukhopadhyay. A survey on shape-constraint
513 deep learning for medical image segmentation. *IEEE Re-
514 views in Biomedical Engineering*, 2021.
- 515 [Bransby *et al.*, 2023] Kit Mills Bransby, Greg Slabaugh,
516 Christos Bourantas, and Qianni Zhang. Joint dense-point
517 representation for contour-aware graph segmentation. *arXiv
518 preprint arXiv:2306.12155*, 2023.
- 519 [Bruse *et al.*, 2017] Jan L Bruse, Maria A Zuluaga, Abbas
520 Khushnood, Kristin McLeod, Hopewell N Ntsinjana, Tain-
521 Yen Hsia, Maxime Sermesant, Xavier Pennec, Andrew M
522 Taylor, and Silvia Schievano. Detecting clinically meaning-
523 ful shape clusters in medical image data: metrics analysis
524 for hierarchical clustering applied to healthy and patho-
525 logical aortic arches. *IEEE Transactions on Biomedical
526 Engineering*, 64(10):2373–2383, 2017.
- 527 [Chen *et al.*, 2002] Yunmei Chen, Hemant D Tagare, She-
528 shadri Thiruvankadam, Feng Huang, David Wilson, Kaun-
529 dinya S Gopinath, Richard W Briggs, and Edward A Geiser.
530 Using prior shapes in geometric active contours in a vari-
531 ational framework. *International Journal of Computer
532 Vision*, 50:315–328, 2002.
- 533 [Chen *et al.*, 2021] Jieneng Chen, Yongyi Lu, Qihang Yu, Xi-
534 angde Luo, Ehsan Adeli, Yan Wang, Le Lu, Alan L Yuille,
535 and Yuyin Zhou. Transunet: Transformers make strong
536 encoders for medical image segmentation. *arXiv preprint
537 arXiv:2102.04306*, 2021.
- 538 [Chen *et al.*, 2023] Gongping Chen, Lei Li, Yu Dai, Jianxun
539 Zhang, and Moi Hoon Yap. Aau-net: An adaptive attention
540 u-net for breast lesions segmentation in ultrasound images.
541 *IEEE Transactions on Medical Imaging*, 42(5):1289–1300,
542 2023.
- 543 [Cootes *et al.*, 1995] Timothy F Cootes, Christopher J Taylor,
544 David H Cooper, and Jim Graham. Active shape models-
545 their training and application. *Computer vision and image
546 understanding*, 61(1):38–59, 1995.
- 547 [Debavelaere *et al.*, 2020] Vianney Debavelaere, Stanley
548 Durrleman, Stéphanie Allasonnière, and Alzheimer’s Dis-
549 ease Neuroimaging Initiative. Learning the clustering of
550 longitudinal shape data sets into a mixture of independent
551 or branching trajectories. *International Journal of Com-
552 puter Vision*, 128:2794–2809, 2020.
- [Feng *et al.*, 2018] Zhen-Hua Feng, Josef Kittler, Muham- 553
554 mad Awais, Patrik Huber, and Xiao-Jun Wu. Wing loss
555 for robust facial landmark localisation with convolutional
556 neural networks. In *Proceedings of the IEEE conference on
557 computer vision and pattern recognition*, pages 2235–2245,
558 2018.
- [Gaggion *et al.*, 2022] Nicolás Gaggion, Lucas Mansilla, 559
560 Candelaria Mosquera, Diego H Milone, and Enzo Ferrante.
561 Improving anatomical plausibility in medical image seg-
562 mentation via hybrid graph neural networks: applications
563 to chest x-ray analysis. *IEEE Transactions on Medical
564 Imaging*, 42(2):546–556, 2022.
- [Gao *et al.*, 2023] Jianxiong Gao, Xuelin Qian, Yikai Wang, 565
566 Tianjun Xiao, Tong He, Zheng Zhang, and Yanwei Fu.
567 Coarse-to-fine amodal segmentation with shape prior. In
568 *Proceedings of the IEEE/CVF International Conference on
569 Computer Vision*, pages 1262–1271, 2023.
- [He *et al.*, 2016] Kaiming He, Xiangyu Zhang, Shaoqing 570
571 Ren, and Jian Sun. Deep residual learning for image recog-
572 nition. In *Proceedings of the IEEE conference on computer
573 vision and pattern recognition*, pages 770–778, 2016.
- [Jiang and Veeraraghavan, 2022] Jue Jiang and Harini Veer- 574
575 araghavan. One shot pacs: Patient specific anatomic context
576 and shape prior aware recurrent registration-segmentation
577 of longitudinal thoracic cone beam cts. *IEEE Transactions
578 on Medical Imaging*, 41(8):2021–2032, 2022.
- [Kuo *et al.*, 2019] Weicheng Kuo, Anelia Angelova, Jitendra 579
580 Malik, and Tsung-Yi Lin. Shapemask: Learning to segment
581 novel objects by refining shape priors. In *Proceedings of
582 the IEEE/CVF international conference on computer vision*,
583 pages 9207–9216, 2019.
- [Lee *et al.*, 2019] Matthew Chung Hai Lee, Kersten Petersen, 584
585 Nick Pawlowski, Ben Glocker, and Michiel Schaap. Tetris:
586 Template transformer networks for image segmentation
587 with shape priors. *IEEE transactions on medical imaging*,
588 38(11):2596–2606, 2019.
- [Li *et al.*, 2017] Yuanwei Li, Chin Pang Ho, Matthieu Toule- 589
590 monde, Navtej Chahal, Roxy Senior, and Meng-Xing
591 Tang. Fully automatic myocardial segmentation of contrast
592 echocardiography sequence using random forests guided
593 by shape model. *IEEE transactions on medical imaging*,
594 37(5):1081–1091, 2017.
- [Li *et al.*, 2019] Cheng Li, Hui Sun, Zaiyi Liu, Meiyun Wang, 595
596 Hairong Zheng, and Shanshan Wang. Learning cross-modal
597 deep representations for multi-modal mr image segmenta-
598 tion. In *Medical Image Computing and Computer Assisted
599 Intervention–MICCAI 2019: 22nd International Confer-
600 ence, Shenzhen, China, October 13–17, 2019, Proceedings,
601 Part II 22*, pages 57–65. Springer, 2019.
- [Li *et al.*, 2022] Zhixuan Li, Weining Ye, Tingting Jiang, and 602
603 Tiejun Huang. 2d amodal instance segmentation guided
604 by 3d shape prior. In *European Conference on Computer
605 Vision*, pages 165–181. Springer, 2022.
- [Li *et al.*, 2023] Zhixuan Li, Weining Ye, Tingting Jiang, and 606
607 Tiejun Huang. Gin: Generative invariant shape prior for

- 608 amodal instance segmentation. *IEEE Transactions on Mul-*
609 *timedia*, 2023.
- 610 [Medley *et al.*, 2019] Daniela O Medley, Carlos Santiago,
611 and Jacinto C Nascimento. Deep active shape model for ro-
612 bust object fitting. *IEEE Transactions on Image Processing*,
613 29:2380–2394, 2019.
- 614 [Milletari *et al.*, 2017] Fausto Milletari, Alex Rothberg,
615 Jimmy Jia, and Michal Sofka. Integrating statistical prior
616 knowledge into convolutional neural networks. In *Medi-*
617 *cal Image Computing and Computer Assisted Intervention-*
618 *MICCAI 2017: 20th International Conference, Quebec City,*
619 *QC, Canada, September 11-13, 2017, Proceedings, Part I*
620 *20*, pages 161–168. Springer, 2017.
- 621 [Nosrati *et al.*, 2016] Nosrati, Masoud S, Hamarneh, and
622 Ghassan. Incorporating prior knowledge in medical image
623 segmentation: a survey. *arXiv preprint arXiv:1607.01092*,
624 2016.
- 625 [Oktay *et al.*, 2018] Ozan Oktay, Jo Schlemper, Loic Le Fol-
626 goc, Matthew Lee, Mattias Heinrich, Kazunari Misawa,
627 Kensaku Mori, Steven McDonagh, Nils Y Hammerla, Bern-
628 hard Kainz, et al. Attention u-net: Learning where to look
629 for the pancreas. *arXiv preprint arXiv:1804.03999*, 2018.
- 630 [Ronneberger *et al.*, 2015] Olaf Ronneberger, Philipp Fis-
631 cher, and Thomas Brox. U-net: Convolutional networks for
632 biomedical image segmentation. In *Medical Image Com-*
633 *puting and Computer-Assisted Intervention–MICCAI 2015:*
634 *18th International Conference, Munich, Germany, Octo-*
635 *ber 5-9, 2015, Proceedings, Part III 18*, pages 234–241.
636 Springer, 2015.
- 637 [Schoenemann *et al.*, 2007] Schoenemann, Thomas, Cre-
638 mers, and Daniel. Globally optimal image segmentation
639 with an elastic shape prior. In *2007 IEEE 11th International*
640 *Conference on Computer Vision*, pages 1–6. IEEE, 2007.
- 641 [Shen *et al.*, 2013] Wei Shen, Yan Wang, Xiang Bai,
642 Hongyuan Wang, and Longin Jan Latecki. Shape clus-
643 tering: Common structure discovery. *Pattern Recognition*,
644 46(2):539–550, 2013.
- 645 [Shiraishi *et al.*, 2000] Junji Shiraishi, Shigehiko Katsura-
646 gawa, Junpei Ikezoe, Tsuneo Matsumoto, Takeshi
647 Kobayashi, Ken-ichi Komatsu, Mitate Matsui, Hiroshi Fu-
648 jita, Yoshie Kodera, and Kunio Doi. Development of a
649 digital image database for chest radiographs with and with-
650 out a lung nodule: receiver operating characteristic analysis
651 of radiologists’ detection of pulmonary nodules. *American*
652 *Journal of Roentgenology*, 174(1):71–74, 2000.
- 653 [Song *et al.*, 2020] Youyi Song, Lei Zhu, Baiying Lei, Bin
654 Sheng, Qi Dou, Jing Qin, and Kup-Sze Choi. Shape mask
655 generator: Learning to refine shape priors for segmenting
656 overlapping cervical cytoplasm. In *Medical Image Com-*
657 *puting and Computer Assisted Intervention–MICCAI 2020:*
658 *23rd International Conference, Lima, Peru, October 4–8,*
659 *2020, Proceedings, Part IV 23*, pages 639–649. Springer,
660 2020.
- 661 [Srivastava *et al.*, 2005] Anuj Srivastava, Shantanu H Joshi,
662 Washington Mio, and Xiuwen Liu. Statistical shape analy-
663 sis: Clustering, learning, and testing. *IEEE Transactions on*
pattern analysis and machine intelligence, 27(4):590–602,
2005.
- [Sun *et al.*, 2020] Jesse Sun, Fatemeh Darbehani, Mark Zaidi,
and Bo Wang. Saunet: Shape attentive u-net for inter-
pretable medical image segmentation. In *Medical Image*
Computing and Computer Assisted Intervention–MICCAI
2020: 23rd International Conference, Lima, Peru, Octo-
ber 4–8, 2020, Proceedings, Part IV 23, pages 797–806.
Springer, 2020.
- [Valanarasu *et al.*, 2022] Valanarasu, Jeya Maria Jose, Patel,
and Vishal M. Unext: Mlp-based rapid medical image seg-
mentation network. In *International Conference on Medi-*
cal Image Computing and Computer-Assisted Intervention,
pages 23–33. Springer, 2022.
- [Xing *et al.*, 2015] Fuyong Xing, Yuanpu Xie, and Lin Yang.
An automatic learning-based framework for robust nucleus
segmentation. *IEEE transactions on medical imaging*,
35(2):550–566, 2015.
- [Zhao *et al.*, 2021] Chen Zhao, Yan Xu, Zhuo He, Jinshan
Tang, Yijun Zhang, Jungang Han, Yuxin Shi, and Weihua
Zhou. Lung segmentation and automatic detection of covid-
19 using radiomic features from chest ct images. *Pattern*
Recognition, 119:108071, 2021.
- [Zheng *et al.*, 2021] Sixiao Zheng, Jiachen Lu, Hengshuang
Zhao, Xiatian Zhu, Zekun Luo, Yabiao Wang, Yanwei Fu,
Jianfeng Feng, Tao Xiang, Philip HS Torr, et al. Rethink-
ing semantic segmentation from a sequence-to-sequence
perspective with transformers. In *Proceedings of the*
IEEE/CVF conference on computer vision and pattern
recognition, pages 6881–6890, 2021.
- [Zhou *et al.*, 2020] Zongwei Zhou, Md Mahfuzur Rahman
Siddiquee, Nima Tajbakhsh, and Jianming Liang. Unet++:
Redesigning skip connections to exploit multiscale features
in image segmentation. *IEEE Transactions on Medical*
Imaging, 39(6):1856–1867, 2020.